

The Application of Ligand-Mapping Molecular Dynamics Simulations to the Rational Design of Peptidic Modulators of Protein–Protein Interactions

Yaw Sing Tan,^{†,‡} David R. Spring,[†] Chris Abell,[†] and Chandra S. Verma^{*,‡,§,⊥}

[†]Department of Chemistry, University of Cambridge, Lensfield Road, Cambridge CB2 1EW, United Kingdom

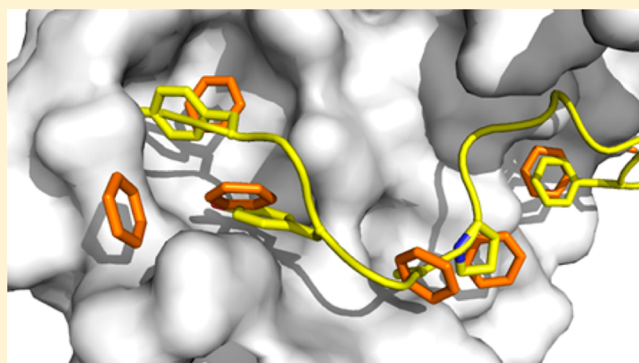
[‡]Bioinformatics Institute (A*STAR), 30 Biopolis Street, #07-01 Matrix, Singapore 138671

[§]Department of Biological Sciences, National University of Singapore, 14 Science Drive 4, Singapore 117543

[⊥]School of Biological Sciences, Nanyang Technological University, 60 Nanyang Drive, Singapore 637551

Supporting Information

ABSTRACT: A computational ligand-mapping approach to detect protein surface pockets that interact with hydrophobic moieties is presented. In this method, we incorporated benzene molecules into explicit solvent molecular dynamics simulations of various protein targets. The benzene molecules successfully identified the binding locations of hydrophobic hot-spot residues and all-hydrocarbon cross-links of known peptidic ligands. They also unveiled cryptic binding sites that are occluded by side chains and the protein backbone. Our results demonstrate that ligand-mapping molecular dynamics simulations hold immense promise to guide the rational design of peptidic modulators of protein–protein interactions, including that of stapled peptides, which show promise as an exciting new class of cell-penetrating therapeutic molecules.



INTRODUCTION

Protein–protein interactions (PPIs) have emerged as attractive drug discovery targets in recent years due to their key roles in mediating various cellular functions.^{1,2} PPIs are however notoriously challenging to target. The interfaces that characterize PPIs are often large, shallow, and highly flexible, making rational drug design difficult.^{3,4} Nevertheless, there is growing interest in exploring these, particularly through harnessing peptides as PPI-targeting drugs due to their potency, high specificity, and low toxicity.⁵ Peptides are also viewed as a bridging class of drugs that could potentially combine the desirable properties of small molecules with those of biologics.⁶ Despite numerous successful examples of peptide-based drugs that have already reached the market,⁵ peptides are often considered poor drug candidates because of their low bioavailability, rapid elimination, poor in vivo stability, and parenteral-only administration.⁷ These limitations are now gradually being mitigated by advances in peptide delivery^{8–10} and synthetic methodologies.^{11–13}

An important advance in the development of peptide-based drugs is the introduction of the “stapling” strategy. This entails the introduction of two unnatural α,α -disubstituted residues bearing olefin side chains of varying lengths into a peptide α -helix, followed by a ruthenium-catalyzed ring-closing metathesis reaction¹⁴ to form the staple across one or two α -helical turns. Peptides that have their α -helical structure stabilized by such all-hydrocarbon staples exhibit improvements in helicity,

protease resistance, potency, and cell permeability, making them suitable pharmacological candidates for the inhibition of PPIs.¹⁵ Various studies have demonstrated the therapeutic potential of stapled peptides in the treatment of cancer, specifically by inhibiting the NOTCH transcription factor complex, reactivating the p53 tumor suppressor pathway, and promoting B-cell lymphoma 2 (Bcl-2)-mediated apoptosis.^{16–18} They have also shown potential as therapeutic agents for other diseases such as HIV,^{19,20} diabetes,²¹ cardiovascular disease,²² and respiratory infection.²³ The all-hydrocarbon staple is able to enhance the binding affinity of a peptide for a protein not only by reducing the entropic penalty but also by forming favorable hydrophobic contacts with the protein surface.²⁴ Hence, staples that interact with the protein surface are generally more desirable than those that point into the bulk solvent (Figure 1).

The design of inhibitory stapled peptides requires knowledge of the hot spots^{25,26} of interactions that contribute the bulk of the free energy of association and optimal staple positions.^{15,27} Various computational methods have been developed to rapidly identify binding sites on protein surfaces in the last couple of decades. The earliest methods were either geometry-based or energy-based, such as POCKET²⁸ and GRID,²⁹ respectively. More recently, several knowledge-based methods that make use

Received: November 26, 2014

Published: June 7, 2015

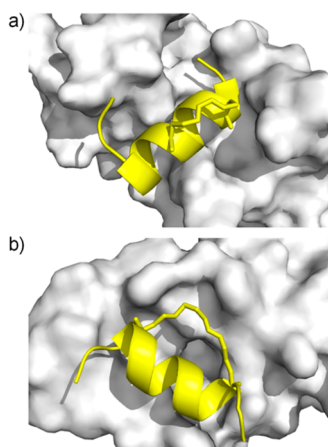


Figure 1. Two types of stapled peptides (yellow) bound to their target proteins (white surface). (a) Hydrocarbon staple points into bulk solvent and does not interact with the surface of HIV-1 capsid (PDB 2L6E). (b) Hydrocarbon staple interacts with the surface of MDM2 (PDB 3V3B).

of the characteristic attributes of protein binding sites, whether it be sequence,³⁰ structural,³¹ or physical,³² have emerged to provide an alternative approach to binding-site detection. A common limitation of these pocket detection methods is that they only treat static structures, and therefore, their success and applicability to drug design are highly dependent upon the input protein structures. However, proteins are intrinsically flexible and frequently undergo conformational changes on ligand binding.^{33,34} The use of a static structure for binding site prediction is therefore highly inadequate, although some progress has been made by adapting these methods for the analysis of conformational ensembles.^{35,36} In contrast, computational methods that employ small-molecule probes in molecular dynamics (MD) simulations are able to account for protein dynamics and have been shown to be quite successful at identifying ligand-binding sites.^{37–43} Various ligands, selected based on their druglike features and prevalence as substructures in drug molecules, are used as binding-site probes to generate ligand affinity maps.^{44,45} These affinity maps were then validated by comparison with crystallographic data of proteins bound to small-molecule ligands, indicating their potential utility for structure-based drug design. However, a framework specific for the design of inhibitory linear and stapled peptides is currently lacking. Some of the probe ligands used, such as benzene, propane and isopropanol, resemble certain chemical moieties found in peptides and have the potential to mimic most inter-residue interactions during the simulations. Therefore, we set out to explore a general protocol for the mapping of peptide binding sites.

We have previously implemented ligand-mapping MD simulations to design a high-affinity hybrid ligand comprising peptide and small-molecule moieties to target an oncogenic protein.³⁹ In this current study, we propose and demonstrate that ligand-mapping MD simulations can also be used for the rational design of peptidic PPI modulators and their stapled variants. Three proteins involved in key PPIs relevant to cancer therapy were selected to validate the method's ability to map peptide binding sites: Aurora-A, RAD51, and MDM2. All three have multiple known hydrophobic hot spots. MDM2 in particular has its binding cleft occluded by the protein backbone in the unbound state, thus providing a rigorous test of the method's ability to uncover buried peptide binding sites. We further applied the ligand-mapping method on five proteins for which close association of the hydrocarbon staple of a stapled peptide

with the protein surface is observed in the crystal structures of the complexes. These included MCL-1 bound to MCL-1 SAHB_D,⁴⁶ estrogen receptor alpha (ER α) bound to SP2, estrogen receptor beta (ER β) bound to SP1,⁴⁷ MDM2 bound to SAH-p53–8,⁴⁸ and MDMX bound to ATSP-7041.⁴⁹

METHODS

Preparation of Structures. Initial protein structures for ligand-mapping MD simulations were obtained from the Protein Data Bank (PDB). The following structures were used: 1OLS⁵⁰ (Aurora-A bound to TPX2), 1OL7⁵⁰ (unbound form of Aurora-A), 1NOW⁵¹ (RAD51-BRC4 fusion protein), 1Z1M⁵² (solution structure of unbound MDM2), 3KJ0⁵³ (MCL-1 complexed with BH3 peptide Bim I2dY), 2QGT⁵⁴ (ER α complexed with nuclear receptor [NR] coactivator 2 peptide and ether estradiol), 3OLS⁵⁵ (ER β complexed with NR coactivator 1 peptide and estradiol), 1YCR⁵⁶ (MDM2 complexed with p53 transactivation domain peptide) and 3FDO⁵⁷ (MDMX complexed with the peptide pDI). Peptidic ligands, if present, were removed to generate the unbound structures, while crystallographic water molecules were retained. The methoxy group of ether estradiol in the ER α structure was removed to convert it to estradiol.

Four N-terminal residues including Arg126, which interacts with TPX2, are missing from the crystal structure of unbound Aurora-A (PDB code 1OL7). They were added following structural alignment with the crystal structure of TPX2-bound Aurora-A (PDB code 1OLS). RAD51 is covalently bound to BRC4 in the crystal structure of the complex, forming a fusion protein. The unbound RAD51 structure was prepared by deleting the BRC4, linker, and expression vector sequences, mutating the selenomethionine residues to methionine and modeling two missing loops using the ModLoop web server.⁵⁸ For MDM2, the second NMR model, in which the p53-binding site is most occluded by the N-terminal lid region, was chosen as the starting structure for the simulations. Two N-terminal residues were removed from the MCL-1 structure as they are not part of the wild-type sequence. Chain B of the ER α structure and chain A of the ER β structure were chosen for the simulations as they are most well-resolved. Missing loops in ER α (residues 462–466) and ER β (residues 416–420) were added using the ModLoop web server.⁵⁸ The point mutation Y537S in the ER α crystal structure was reversed. All proteins were capped by acetyl and N-methyl groups, if either the first or last residue is missing.

The software package PDB2PQR⁵⁹ was used to choose optimal Asn, Gln, and His side-chain orientations, add missing hydrogen atoms, and determine the protonation states of residues. Ten different placements of benzenes around the protein were generated using Packmol,⁶⁰ followed by neutralization with sodium or chloride ions and solvation with TIP3P⁶¹ water molecules in a periodic truncated octahedron box, giving a final benzene concentration of ~ 0.2 M.

Molecular Dynamics. Energy minimizations and MD simulations were performed with the sander and PMEMD modules of AMBER11,⁶² using the ff99SB-ILDN⁶³ force field for the protein and the generalized AMBER force field (GAFF)⁶⁴ for the benzenes. Atomic charges for benzene and estradiol were derived using the R.E.D. Server,⁶⁵ by fitting restrained electrostatic potential (RESP) charges⁶⁶ to a molecular electrostatic potential (MEP) computed by the Gaussian 09 program⁶⁷ at the HF/6-31G* level of theory. Parameters for ADP were used as described by Meagher et al.⁶⁸ The SHAKE algorithm⁶⁹ was used to constrain all bonds involving hydrogen atoms, allowing for a time step of 2 fs. Nonbonded interactions were truncated at 9 Å, and the particle mesh Ewald

method⁷⁰ was used to calculate long-range electrostatic interactions under periodic boundary conditions. With positional restraints on the protein atoms, 500 cycles of steepest descent and 500 cycles of conjugate gradient energy minimizations were performed followed by two 50 ps equilibration MD runs, in which the system was first heated gradually to 300 K at constant volume and then equilibrated at a constant pressure of 1 atm. Subsequent unrestrained equilibration (2 ns) and production runs were performed at constant temperature (300 K) using a Langevin thermostat⁷¹ with a collision frequency of 2 ps⁻¹ and constant pressure (1 atm) using the Berendsen barostat⁷² with a pressure relaxation time of 2 ps. Production time for the ligand-mapping MD simulations was 5 ns, for a cumulative sampling time of 50 ns per protein. Standard MD simulations were performed on the unbound forms of RAD51 and MDM2 for 50 and 200 ns, respectively.

A cubic solvent box containing 40 benzene molecules and 9200 water molecules was generated using Packmol with a distance tolerance of 2 Å. This benzene/water ratio (1:230) is close to the benzene/water ratios observed in the ligand-mapping solvent boxes and corresponds to a benzene concentration of 0.23 M at 300 K and 1 atm. The benzene–water solvent box was subject to the same minimization, equilibration, and production steps as described above for the ligand-mapping solvent boxes but without any atomic restraints imposed. The carbon–carbon radial distribution function (RDF) for the benzene molecules during the first and last 5 ns of the 20 ns production MD simulation was calculated with a bin size of 0.1 Å using the radial command in ptraj.

Trajectory Analysis. For each protein, the 10 individual ligand-mapping MD runs were combined into a single trajectory for analysis. Benzene occupancy grids were generated using the ptraj module of AMBER 11 to bin carbon atoms of benzenes into 1 × 1 × 1 Å grid cells. The cutoff isocontour value used for visualization of benzene occupancy was 3 times the threshold bulk value, which was defined as the highest isovalue at which benzenes were detected in the bulk solvent. This is an arbitrary criterion that allows for the removal of most weak binding sites. To compare the overlap of the benzene occupancy maps with peptide residues, the peptide-bound protein structures were aligned using PyMOL⁷³ to the average protein structure sampled during the simulations. Because of the highly plastic nature of the BH3 binding site in MCL-1 (Supporting Information, Figure S1),⁷⁴ protein structures were aligned with only the binding site residues instead of the entire protein.

Peptide Design. A stapled peptide targeting MCL-1, MCL-1 SAHB_{8–12}, was designed based on benzene occupancy maps obtained from the ligand-mapping MD simulations. The structure of MCL-1 bound to the stapled peptide MCL-1 SAHB_D (PDB code 3MK8)⁴⁶ was used to model the complex between MCL-1 and MCL-1 SAHB_{8–12}. The unresolved MCL-1 loop (residues 194–201) was added using the ModLoop web server.⁵⁸ MCL-1 SAHB_D was then mutated into MCL-1 SAHB_{8–12} by using the tleap module of AMBER 11 to introduce an *i*, *i* + 4 staple at residues 8 and 12 and revert residues 17 and 21 to Gln and Glu, respectively. Atomic charges for the stapled residues were derived using the R.E.D. Server, as described above. The two stapled peptide complexes of MCL-1 were each subject to three independent explicit-solvent MD simulations using different initial atomic velocities for 50 ns. The ff99SB-ILDN⁶³ and GAFF⁶⁴ force fields were used to describe the stapled residues during the simulations. Both stapled peptides were capped by acetyl and N-methyl groups at their N- and C-termini, respectively.

Molecular Mechanics/Poisson–Boltzmann Surface Area. Binding free energies for the two MCL-1 complexes were calculated

using the molecular mechanics/Poisson–Boltzmann surface area (MM/PBSA) method.⁷⁵ Two hundred equally spaced snapshot structures were extracted from the last 40 ns of each of the trajectories, and their molecular mechanical energies were calculated with the sander module. The polar contribution to the solvation free energy was calculated by the pbsa⁷⁶ module, while the non-polar contribution was estimated from the solvent accessible surface area (SASA) using the molsurf⁷⁷ program with $\gamma = 0.00542$ kcal/Å² and $\beta = 0.92$ kcal/mol. Entropies were estimated by normal-mode analysis⁷⁸ using the nmode module. All programs used for MM/PBSA calculations were from AMBER 11.⁶²

Binding Free Energy Decomposition. The contribution of each peptide residue to the binding free energy of the two MCL-1 complexes was computed using the free energy decomposition method⁷⁹ on 200 structures extracted from the last 40 ns of the respective complex trajectories. Similar to the MM/PBSA calculations, the molecular mechanical energies and polar contribution to solvation free energy were computed by the sander and pbsa modules of AMBER 11,⁶² respectively. The nonpolar contribution to solvation free energy was estimated from the SASA using the ICOSA method.⁸⁰

RESULTS AND DISCUSSION

According to a comprehensive analysis of experimental alanine scanning data, PPI hot spots are enriched in tryptophan, arginine, tyrosine, and isoleucine residues.²⁶ Interactions between hydrophobic residues also dominate protein–protein interfaces.⁸¹ Benzene is representative of the aromatic residues, has high affinity for the nonpolar residues, and additionally, can interact with positively charged residues through cation– π and hydrophobic interactions. It was therefore selected as the ligand of choice for the mapping of peptide-binding sites in this study.

We followed the same protocol for performing ligand-mapping MD simulations as previously described.³⁹ For each target protein, 10 independent 5 ns MD simulations with different initial benzene distributions were performed in explicit solvent for a total sampling time of 50 ns. No restraints were placed on the protein atoms to allow for maximal and accurate hot-spot sampling within the short simulation period.⁴² A low benzene concentration of 0.2 M was used to minimize ligand aggregation. We confirmed that this is a suitable concentration by assessing the carbon–carbon RDF for the benzene molecules in an MD simulation of a benzene–water solvent box (1 benzene molecule to 230 water molecules), which converged toward unity within the van der Waals cutoff of 9 Å (Supporting Information, Figure S2a). RDFs are recommended for the evaluation of appropriate solvent behavior in such MD-based mapping techniques, whereby proper mixing of the probes and water is indicated by convergence of the RDF to 1 at long probe–probe distances, while convergence of the RDF to values well above 1 indicates phase separation.⁸² No evidence of phase separation was observed in the benzene–water mixture for up to 20 ns (Supporting Information, Figure S2b).

Aurora-A. Aurora-A is a serine/threonine kinase involved in the assembly and maintenance of the mitotic spindle. It is over-expressed in a variety of human cancers, indicating that it may be a valid oncogenic drug target.⁸³ The microtubule-binding protein TPX2 locks Aurora-A in the active conformation by binding to its C-terminal domain at two distinct sites.⁵⁰ Cheng et al.⁸⁴ have used free energy decomposition analysis to show that the majority of the binding free energy is contributed by hydrophobic residues from TPX2, making this system suitable for validation of the ligand-mapping method. Two sets of

ligand-mapping MD simulations were performed using the unbound protein conformations derived from the crystal structures of Aurora-A (PDB code 1OL7) and Aurora-A/TPX2 complex (PDB code 1OLS) as the initial structures. The ADP cofactor was left intact in its pocket in both structures to allow the benzenes to probe for surface binding sites only.

Both sets of simulations yielded very similar benzene occupancy maps (Figure 2). Almost all of the binding sites occupied by the

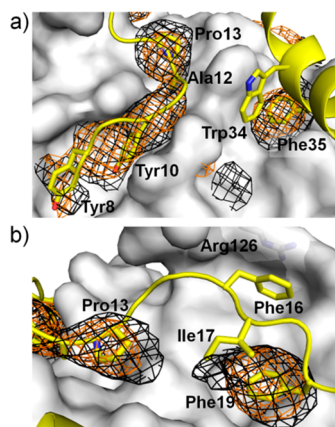


Figure 2. Benzene occupancy maps of Aurora-A (white surface) with TPX2 peptide (yellow) superimposed. Regions visited by benzenes are represented as black (initial protein conformation derived from unbound structure) and orange (initial protein conformation derived from TPX2-bound structure) meshes. (a) Benzene probes reproduce hydrophobic interactions of TPX2 residues 7–13 and 31–43. (b) Benzene probes reproduce hydrophobic interactions of TPX2 residues 13–21 but not the cation– π interaction of Phe16 with Arg126.

hydrophobic TPX2 residues were detected by the benzenes. Both the hydrophobic groove accommodating Tyr8, Tyr10, Ala12, and Pro13 and the neighboring pocket binding Ile17 and Phe19 have high benzene occupancy. The cation– π interactions between Phe16 and Arg126 from Aurora-A were, however, not reproduced in the simulations (Figure 2b). Because of the flexibility of the N-terminus in the Aurora-A structures and the loss of constraints imposed by lattice crystal contacts, it was very likely that Arg126 drifted away shortly after the simulations started, thus disassembling the binding site before a benzene molecule could arrive to interact with it. In addition, molecular mechanical force fields do not describe quadrupolar electrostatic interactions, which form the basis for cation– π interactions.⁸⁵ Cation– π interaction energies computed using a nonpolarizable AMBER force field have been shown to be significantly underestimated compared to those obtained by *ab initio* quantum mechanical calculations.⁸⁶ The lack of benzene density near Arg126 could therefore also be attributed to force-field limitations.

At the downstream helical stretch of TPX2, the location of Phe35 was recapitulated in the benzene affinity maps (Figure 2a). However, the adjoining Trp34 binding site was only partially mapped. The Trp34 side chain is tethered to the TPX2 peptide backbone, allowing it to engage in π – π stacking interactions with a histidine residue from Aurora-A. In contrast, benzene probes are untethered and therefore unable to dwell at such an exposed and ill-defined binding site for long. Nevertheless, it is clear that the ligand-mapping method has proven useful in identifying the major TPX2 binding sites on Aurora-A.

RAD51. RAD51 is a recombinase involved in the repair of DNA double-strand breaks^{87–89} and is often overexpressed

in cancer cells.^{90–92} Its function is regulated by the tumor suppressor breast cancer type 2 susceptibility protein (BRCA2). The interaction between BRCA2 and RAD51 is mediated mainly by eight highly conserved motifs called the BRC repeats, each having ~ 35 residues and varying affinity for RAD51.^{93,94} The only available crystal structure of human RAD51 consists of its C-terminal domain joined to BRC repeat 4 (BRC4) by a linker peptide,⁵¹ and this structure was used for the simulations.

BRC4 is made up of a β -hairpin at its N-terminal half that extends the β -sheet of RAD51 by two antiparallel strands and an α -helical segment at its C-terminal half. The interface between the β -hairpin and RAD51 is similar to the RAD51 oligomeric interface.⁵¹ Two four-residue modules in the BRC repeats known as the FXXA and LFDE modules have been identified to be essential for binding to RAD51.⁹⁵ Four of the modular residues, namely, Phe1524, Ala1527, Leu1545, and Phe1546, interact with hydrophobic pockets on the RAD51 surface. The positions of these four residues, as well as those of Ile1534 and Val1542, were successfully mapped by the benzenes in the ligand-mapping MD simulations (Figure 3a). These residues have been previously identified by computational alanine scanning to contribute significantly to the binding free energy.⁹⁶ This shows once again that the ligand-mapping strategy is able to establish peptide-binding hot spots on proteins.

Inspection of the benzene occupancies in the vicinity of the FXXA module revealed three neighboring benzene binding sites (Figure 3b). These binding sites could prove useful for improving the potency of the tetrapeptide FHTA, which has been shown to bind to a humanized RadA mutant at the FXXA region with weak micromolar affinity.⁹⁷ Benzene density (green circle in Figure 3b) was observed beneath the RAD51 surface near the Ala1527 pocket. This indicated that some ligand-induced movement of the protein had occurred. Indeed, the RAD51 $\alpha 4$ helix had shifted away from the Ala1527 pocket in one of the ligand-mapping MD simulations to reveal an auxiliary channel that effectively enlarges the pocket (Figure 3c,d). The walls of this binding channel comprise Leu171, Leu172, Val185, and Leu186. To confirm that this was not a chance occurrence, the 10 ligand-mapping MD simulations of RAD51 were extended to 20 ns each. The binding site revealed itself again in another simulation run after 13 ns. However, this cryptic binding site did not appear in a 50 ns benzene-free simulation of RAD51. This agrees with previous observations that the inclusion of ligands in MD simulations increases the conformational sampling of proteins.^{39,41} In this case specifically, it has been shown that ligand-mapping MD simulations are also able to reveal binding sites that are blocked by the protein backbone.

MDM2 Solution Structure. It has been demonstrated previously that ligand-mapping MD simulations are able to identify cryptic binding sites occluded by protein side chains.³⁹ Typically, the time scale for protein backbone movement is longer than for side-chain rotation since the former involves the displacement of many more atoms.⁹⁸ Here, we sought to test the capability of ligand-mapping MD simulations to map binding sites that are occluded by the protein backbone. We have already seen that benzene ligands are able to induce backbone movement in RAD51 to enlarge a known pocket; however, this has not been demonstrated experimentally yet. So we chose the protein MDM2, which is known to bind to p53 and regulate its stability, thus making it a validated target in cancer therapy.⁹⁹ The transactivation domain of p53 binds as an amphipathic α -helix to a deep hydrophobic cleft on the N-terminal domain of MDM2 (Supporting Information, Figure S3a). Site-directed

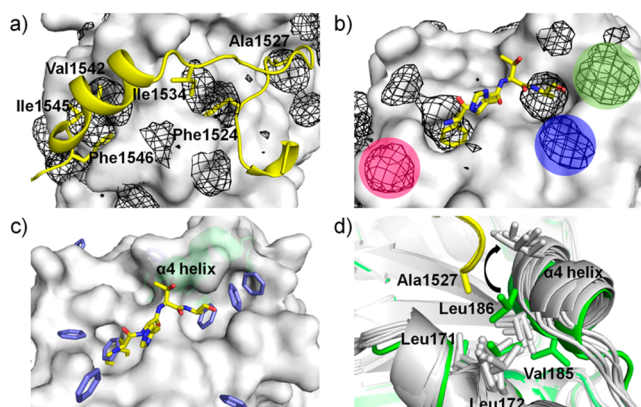


Figure 3. (a) Benzene occupancy map of RAD51 (white surface) with BRC4 peptide (yellow) superimposed. Regions visited by benzenes are represented as black mesh. The benzene probes reproduced crucial hydrophobic interactions between BRC4 (residues labeled) and RAD51. (b) Three benzene binding sites proximal to the FXXA pockets. (c) Single trajectory structure from ligand-mapping MD simulations. Protein backbone movement induced by benzenes (purple) revealed a cryptic auxiliary channel that enlarged the Ala1527 pocket. (d) Trajectory structures with cryptic binding channel revealed (white) superimposed on the crystal structure of the complex between RAD51 (green) and BRC4 (yellow). Upward movement of the α 4 helix revealed a new binding channel comprising Leu171, Leu172, Val185, and Leu186.

mutagenesis experiments have shown that Phe19, Trp23, and Leu26 of p53 are the three key residues for binding to MDM2.¹⁰⁰ In the unliganded state of MDM2, access to the p53-binding cleft is obstructed by an N-terminal “lid” region (residues 1–24, Supporting Information, Figure S3b).^{52,101} The binding cleft is also shallower and narrower in the unbound state compared to the bound state, expanding through rearrangement of secondary structural elements in response to ligand binding.⁵² We chose the second model of the solution structure of MDM2 (PDB code 1Z1M) for our simulations as its binding cleft is the most occluded by the N-terminal lid.

The p53-binding cleft was successfully mapped by the benzenes in the simulations, including the locations of the hot-spot residues Phe19 and Trp23, but not that of Leu26 (Figure 4a). Located at the base of the N-terminal lid, the Leu26 binding site is the most occluded compared to the Phe19 and Trp23 binding sites. This result is similar to that reported in a previous druggability prediction study that used a mixture of isopropanol, isopropylamine, acetate, and acetamide as probe ligands in MD simulations of the MDM2 solution structure.⁴¹ A previously reported second binding pocket of MDM2³⁸ was also detected in our ligand-mapping MD simulations (Figure 4b). This binding site was occluded in the initial MDM2 structure used for the simulations and was only revealed by the rearrangements of residues Phe86, Glu95, Lys98, and Met102. In addition to these two well-defined binding sites, a third binding site in the region between Tyr100 and Tyr104 was also detected (Figure 4b). This region is very close to where a second nutlin molecule forms a crystal contact with MDM2 in the structure of the MDM2–nutlin-2 complex¹⁰² and has been proposed to be the “landing pad” for nutlin when it encounters MDM2, prior to diffusion to the main pocket.¹⁰³ Titration experiments have shown that the displacement of p53 peptide from MDM2 by nutlin-3 is compromised by a Y104G mutation in MDM2, suggesting that Tyr104 and its surrounding region play a role in nutlin binding. The benzene densities are very close to but do not overlap with the second nutlin molecule in the MDM2/nutlin-2 crystal structure.

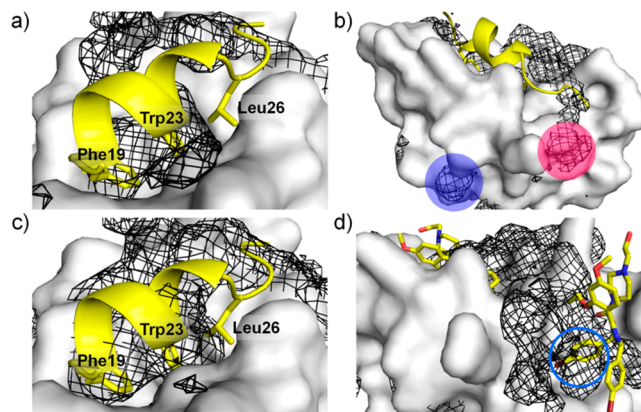


Figure 4. Ligand-mapping MD simulations on the solution structure of MDM2. (a, b) Benzene occupancy maps derived from 5 ns ligand-mapping simulations. (c, d) Benzene occupancy maps derived from 20 ns ligand-mapping simulations. Regions visited by benzenes are represented as black mesh. (a) Benzene probes displaced the N-terminal lid to mimic the interactions of the p53 hot-spot residues Phe19 and Trp23 but not that of Leu26. (b) Two other reported interaction sites were detected by benzene probes. One was identified in previous MD simulation studies (blue) as a putative druggable site, while the other pocket (red) was proposed to be important for initial nutlin-3 binding.¹⁰³ (c) Benzene probes were able to reproduce the hydrophobic interactions of all three hot-spot residues (sticks) in the p53-binding cleft and (d) nutlin-2 at the second nutlin interaction site (circled in blue).

Similar to Leu26, the second nutlin interaction site remained occluded by the N-terminal tail during the 5 ns ligand-mapping MD simulations and was not mapped by the benzene probes. The simulations were extended to 20 ns to see if a longer simulation time would reveal these two binding sites. Both of them were indeed mapped during the extended simulations. The benzene densities now overlap partially with Leu26 (Figure 4c). There was also good overlap between the benzene densities and the nutlin molecule at the second nutlin interaction site (Figure 4d). The benzene occupancy maps constructed from the first 10 and 15 ns of the simulations were also analyzed but found not to overlap with Leu26. Benzene occupancy maps generated from the ligand-mapping MD simulations of RAD51 showed that protein backbone movement induced by ligand binding can be observed within 5 ns. However, the conformational change involved the movement of a relatively short protein stretch comprising fewer than 10 residues. The results suggest that, to observe ligand-induced conformational changes involving long flexible loops, such as the 24-residue N-terminal lid of MDM2, a significantly longer sampling time is required.

It has been reported that the presence of benzene ligands in MD simulations increases the conformational sampling of protein side chains.³⁹ To see if this effect applies to the protein backbone as well, we performed a 200 ns benzene-free MD simulation of the MDM2 solution structure in addition to the ligand-mapping MD simulations. The 10 ligand-mapping trajectories were merged to give a combined trajectory with a cumulative sampling time of 200 ns. Equally spaced snapshots were extracted from these two sets of trajectories for comparison. The N-terminal lid remained closed over the p53-binding cleft throughout the benzene-free simulation, while it was much more dynamic in the ligand-mapping simulations, exploring multiple conformational states and exposing the binding cleft (Supporting Information, Figure S4). This enhancement of sampling extended to the domain core, as the representative ligand-mapping trajectory snapshots showed considerable variation in their secondary structures, in

contrast to the well-aligned trajectory snapshots from the benzene-free simulation.

Hydrocarbon Linker Placement in Stapled Peptides. It is evident from the results described above that ligand-mapping MD simulations can efficiently probe for hydrophobic regions on protein surfaces. We extended the study to investigate the ability of ligand-mapping MD simulations to identify hydrocarbon staple binding sites. To simulate the stapled peptide design process, well-resolved protein structures that are bound to the linear version of the stapled peptides, if available, were selected from the PDB as the initial structures for the simulations.

MDM2 and MDMX. The structure of MDM2 complexed with p53 transactivation domain peptide was chosen, and simulations were performed on the unbound protein structure. The interaction of the hydrocarbon staple of the $i, i + 7$ stapled peptide, SAH-p53-8, with a relatively flat binding platform was reproduced by the benzene probes (Figure 5a). Another

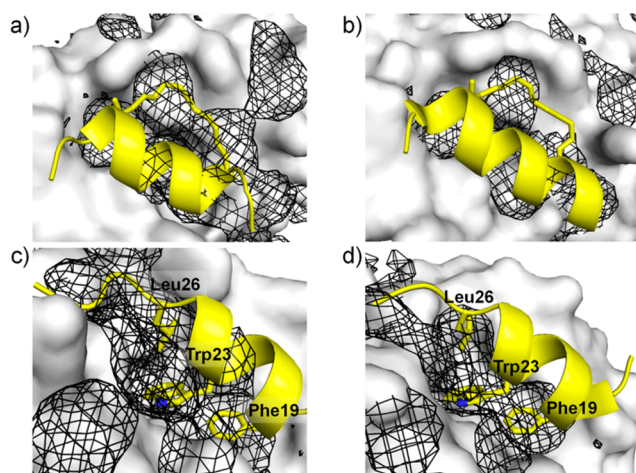


Figure 5. Benzene occupancy maps of MDM2 and MDMX (white surface) with peptides (yellow) superimposed. Regions visited by benzenes are represented as black mesh. Benzene probes reproduce interactions of the hydrocarbon staple with (a) MDM2 (PDB 3V3B) and (b) MDMX (PDB 4N5T). The locations of the p53 core binding triad of Phe19, Trp23, and Leu26 in (c) MDM2 (PDB 1YCR) and (d) MDMX (PDB 3DAB) are also recapitulated in the simulations.

$i, i + 7$ stapled peptide, ATSP-7041, binds to MDMX in a similar manner, with the hydrocarbon staple engaging a flat binding platform adjoining the p53-binding cleft. This interaction was recapitulated in the benzene occupancy map of MDMX, which showed substantial overlap of benzene densities with the hydrocarbon staple (Figure 5b). The benzene densities also coincide with the hydrophobic binding triad of Phe19, Trp23, and Leu26 in the p53-binding clefts of both MDM2 and MDMX (Figure 5c,d).

MCL-1. The antiapoptotic activity of MCL-1 is mediated by a hydrophobic binding groove on its surface that binds the BH3 α -helices of proapoptotic Bcl-2 family proteins. Small-molecule and peptidic inhibitors that target the BH3 binding groove have been developed in an attempt to inhibit MCL-1 for anticancer therapy.¹⁰⁴

The structure of MCL-1 complexed with MCL-1 SAHB_D was the first reported structure of a protein complexed with a stapled peptide.⁴⁶ It also confirmed computational models that predict that a stapled peptide could gain additional affinity by interacting with the hydrophobic surface of the protein via its

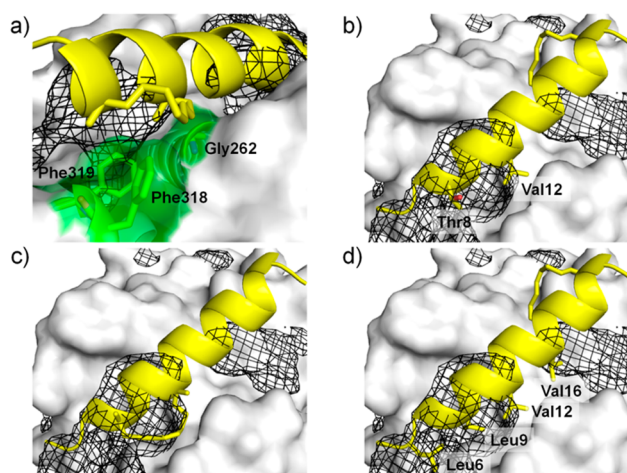


Figure 6. Benzene occupancy maps of MCL-1 (white surface) with stapled peptides (yellow) superimposed. Regions visited by benzenes are represented as black mesh. (a) Benzene probes reproduce hydrophobic interactions of α -methyl group of hydrocarbon staple from MCL-1 SAHB_D with Gly262, Phe319, and Phe318 (green) from MCL-1 (PDB 3MK8). (b) Thr8 and Val12 are indicated by the benzene occupancy map as suitable sites for forming a hydrocarbon staple that interacts with the protein surface. (c) Minimized structure of the complex of MCL-1 with MCL-1 SAHB₈₋₁₂. (d) Benzene probes reproduce interactions of hydrophobic MCL-1 SAHB_D residues (sticks) with MCL-1 at the binding interface.

hydrocarbon staple.²⁴ Figure 6a depicts the hydrophobic contacts that the hydrocarbon staple of MCL-1 SAHB_D makes with MCL-1. A methyl group attached to the backbone α atom of a stapled residue binds in a shallow groove formed by Gly262, Phe318, and Phe319. This interaction was captured in the benzene occupancy map of MCL-1 (Figure 6a). No overlap of the benzene densities with the rest of the hydrocarbon staple was observed, implying that it interacts weakly at this region.

A more favorable region for forming hydrophobic contacts with a hydrocarbon staple was indicated at the N-terminal end of the BH3 peptide by the benzene occupancy maps. His224, Ala227, Phe228, and Met231 form a hydrophobic patch close to Thr8 and Val12 of the peptide, and the high benzene densities here show that hydrophobic interactions with the protein surface are decidedly favorable (Figure 6b). An N-terminal $i, i + 4$ staple linking residues 8 and 12 may be created (Figure 6c) to interact with this binding site, generating a stapled BH3 peptide that could be more potent than the C-terminally stapled MCL-1 SAHB_D. We called this N-terminally stapled peptide MCL-1 SAHB₈₋₁₂. Indeed, this observation agrees with the results from a previous computational study of several stapled BH3 peptides against MCL-1, which showed via extensive staple-scanning MD simulations and free energy analysis that MCL-1 SAHB₈₋₁₂ has a higher binding affinity for MCL-1 than MCL-1 SAHB_D and that the N-terminal staple itself contributes more to the binding compared to the C-terminal staple.¹⁰⁵ We were able to reproduce these findings in multiple independent MD simulations of the two stapled peptide–MCL-1 complexes (Supporting Information, Tables S1 and S2). These show that ligand-mapping MD simulations could complement computationally intensive staple-scanning MD simulations as an alternative means of suggesting suitable stapling sites in the design of stapled peptides. Furthermore, while relatively long staple-scanning simulations are required for binding free energies to converge, each ligand-mapping MD simulation is only 5 ns, leading to considerable savings in computational time.

Figure 6d shows that the benzene probes were able to detect other hydrophobic interactions at the MCL-1–SAHB_D binding interface. The benzene occupancy map demonstrates good overlap with the hydrophobic residues, Leu6, Leu9, Val12, and Val16 of MCL-1 SAHB_D, further corroborating the applicability of ligand-mapping MD simulations to the detection of peptide-binding hot spots.

Estrogen Receptors. Estrogen receptors (ERs) are part of the nuclear receptor superfamily of transcription factors. There are two isoforms of ER: ER α and ER β . They are encoded by different genes but share a high degree of sequence and structural similarity. Both contain a variable N-terminal AF1 domain, a well-conserved DNA binding domain, and a C-terminal ligand binding domain (LBD).¹⁰⁶ Estradiol is an ER agonist that binds to the LBD, causing a conformational change that promotes homodimerization and favors the recruitment of coactivator proteins to the ER/DNA complex.¹⁰⁷ On agonist binding, a coactivator binding groove is created that mediates interactions with short α -helical leucine-rich motifs called the NR box.¹⁰⁸ ER antagonists, however, promote the recruitment of corepressor proteins.¹⁰⁹

X-ray crystal structures of both ER isoforms bound to stapled NR box peptides reveal that the $i, i + 4$ hydrocarbon staples form van der Waals contacts with hydrophobic residues of the coactivator binding groove.⁴⁷ These interactions were recapitulated in the benzene occupancy maps of both ERs (Figure 7).

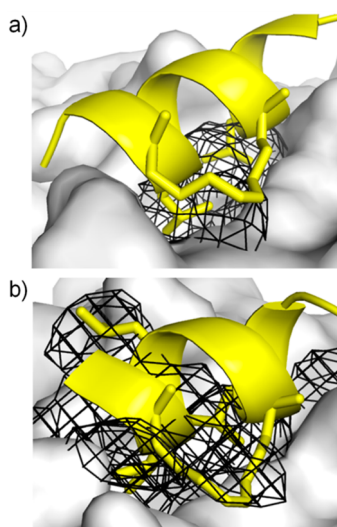


Figure 7. Benzene occupancy maps of ERs (white surface) with stapled NR box peptides (yellow) superimposed. Regions visited by benzenes are represented as black mesh. (a) Benzene probes reproduce interactions of hydrocarbon staple and two leucine residues of a stapled peptide with ER α (PDB 2YJA). (b) Benzene probes reproduce interactions of hydrocarbon staple and three leucine residues of a stapled peptide with ER β (PDB 2YJD).

Other key hydrophobic interactions between leucine residues from the stapled peptides with the ER surfaces were also reproduced in the ligand-mapping MD simulations. Even though the overlap of the benzene densities with the hydrocarbon staple is not as optimal in ER α (Figure 7a) compared to ER β (Figure 7b), the presence of strong benzene densities just beneath the staple nevertheless suggests that this region is suitable for forming van der Waals contacts with a hydrocarbon staple.

Effects of Varying the Cutoff Isovalue. In this study, we consistently used an isovalue 3 times the threshold bulk value to visualize the benzene occupancy grids generated by the ligand-mapping MD simulations. To examine the robustness of this choice, we systematically examined the effect of using higher isovalues for visualization on the mapping of all the test proteins by increasing it to 4 and 5 times the threshold bulk value.

At 4 times the threshold bulk value, significant loss of benzene density was observed in the vicinity of several hot-spot residues, such as Tyr8 of TPX2 (Figure 8a) and Phe1546 of

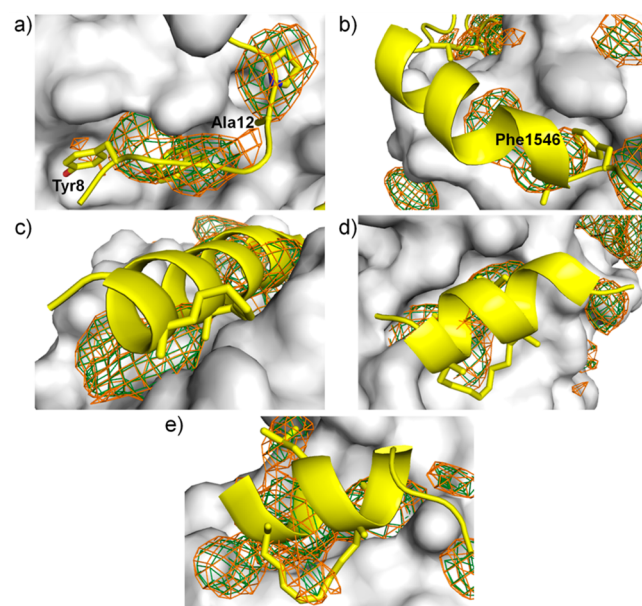


Figure 8. Benzene occupancy maps of (a) Aurora-A with TPX2 peptide superimposed, (b) RAD51 with BRC4 peptide superimposed, (c) MCL-1 with stapled BH3 peptide superimposed, (d) ER α with stapled NR Box peptide superimposed, and (e) ER β with stapled NR box peptide superimposed. Benzene densities were visualized at 4 (orange mesh) and 5 (green mesh) times the threshold bulk isovalue. Proteins and peptides are colored white and yellow, respectively.

BRC4 (Figure 8b). Poor overlap with the benzene maps was generally observed for residues bound at shallow binding sites, such as Ala12 and Ile17 (not shown) of TPX2 on Aurora-A. In the cases of MCL-1 and ER α , the overlap with the hydrocarbon staple was totally lost (Figure 8c,d). At 5 times the threshold bulk value, complete loss of overlap with the relatively solvent-exposed TPX2 hydrophobic hotspots, Tyr8 and Ala12 (Figure 8a), and the hydrocarbon staple of ER β (Figure 8e) was observed. However, overlap of the benzene densities with deep-lying hot-spot residues for all the test proteins remained good.

Nonetheless, when an isovalue of 3 times the threshold bulk value was used to visualize the binding sites, significant regions of the protein surface were still being mapped (Figure 9). We noticed that for Aurora-A and RAD51, proteins which have multiple discrete peptide binding sites, the benzene density clusters that overlap with the known peptide binding hot spots are within the top seven most occupied (Figure 10a,b). For MDM2, MDMX, and MCL-1, their top density clusters are located within their respective peptide-binding grooves (Figure 10c–f), whereas the most-occupied density clusters in ER α and ER β (Figure 10f,g) delineate both their NR box peptide binding sites and dimerization interfaces. This shows that the most important binding hot spots are able to retain their benzene

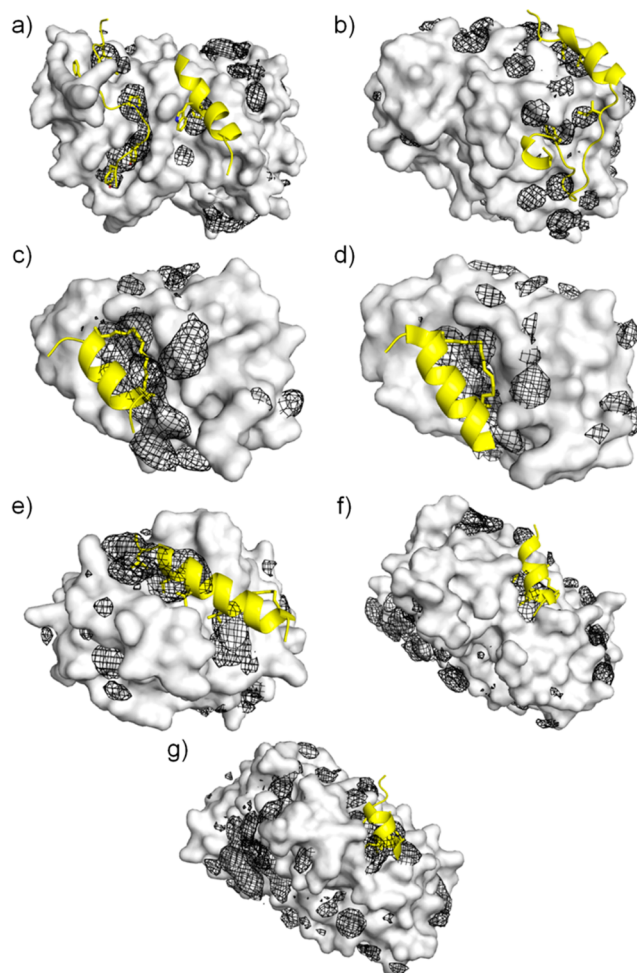


Figure 9. Benzene occupancy maps of (a) Aurora-A, (b) RAD51, (c) MDM2, (d) MDMX, (e) MCL-1, (f) ER α , and (g) ER β superimposed on their peptide-bound structures. Where present, hydrocarbon staples are represented as sticks. Proteins and peptides are colored white and yellow, respectively.

densities at high cutoff isovalues. The ligand-mapping method may therefore potentially be used to unambiguously identify binding hot spots in cases when they are unknown.

A few of the top-ranked binding sites identified in Aurora-A, RAD51, and ER β (Figure 10a,b,g) have not been shown to bind ligands in experimental structures. This begs the question of whether these are bona fide binding sites that have yet to be validated by experiments or just irrelevant false positives. So what is the proper cutoff isovalue to use? For unequivocal visualization of binding hot spots, higher isovalues should be used to interrogate new protein targets which lack structural data of their complexes, and whose binding sites are poorly characterized. However, for established protein targets such as those reported in this study, cryptic and low-affinity binding sites that have not yet been exploited by known ligands are of greater interest. From our study, it is clear that such sites will be missed if isovalues higher than 3 times the threshold bulk value are used for visualization. Judicious selection of the cutoff isovalue is therefore necessary for appropriate interpretation of the data obtained from the ligand-mapping MD simulations; clearly, future developments in such MD-based mapping methods and new experimental data will further help to reduce the ambiguities.

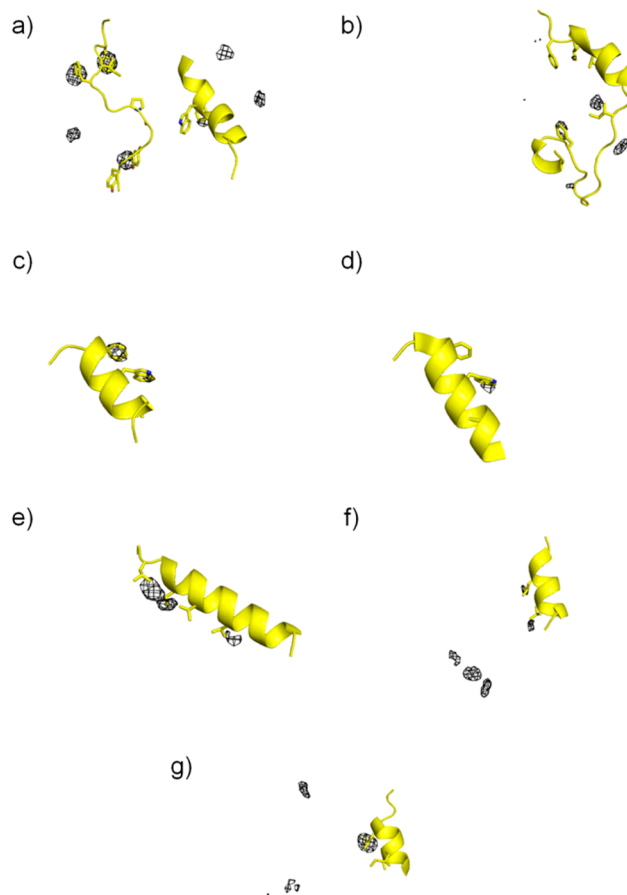


Figure 10. Benzene occupancy maps of (a) Aurora-A, (b) RAD51, (c) MDM2, (d) MDMX, (e) MCL-1, (f) ER α , and (g) ER β superimposed on their respective peptide-bound structures and represented at high isovalues. Key hydrophobic peptide residues are shown as sticks. Proteins were removed for clarity in visualization of the meshes. This figure is of the same scale as that of Figure 9.

CONCLUSION

In this present study, we have demonstrated that the ligand-mapping approach can recapitulate hydrophobic sites on proteins that are exploited for binding by peptidic ligands, thus providing a simple and robust tool to aid the design of novel peptides. We have shown that ligand-mapping MD simulations are able to identify hydrophobic sites used for peptide binding on the surfaces of three therapeutically important proteins, namely, Aurora-A, RAD51, and MDM2.

Significantly, ligand-mapping MD simulations also proved useful for unveiling cryptic binding sites that are occluded by either side chains or the protein backbone. These cryptic binding sites could potentially be exploited for enhancing the binding affinity of known peptide ligands. Standard MD simulations have the potential to expose such sites; however, the time scales involved can be quite long.³⁹ Here we have shown that the ligand-mapping approach, using a hydrophobic probe such as benzene, offers promise in uncovering cryptic binding sites that can then be targeted for inhibition. Simulation lengths as short as 5 ns for each replicate system were sufficient to expose a cryptic site hidden by side chains in MDM2 and another hidden by the protein backbone in RAD51. Indeed, even the 24-residue N-terminal lid region of MDM2 that occludes the p53-binding

cleft was partially displaced. Longer simulations of 20 ns eventually led to the exposure of the Leu26 binding site, which is the most buried among the three hot spots in the p53-binding cleft of the MDM2 solution structure. We therefore recommend that simulation length be increased to at least 20 ns for NMR-resolved protein solution structures, which tend to have longer and a higher number of flexible loops, and therefore require longer sampling times to ensure adequate exploration of any ligand-binding conformations that may be accessed only by protein backbone changes. However, in general, a production time of 5 ns appears to suffice for the mapping of protein X-ray crystal structures. The method's computational feasibility may be further enhanced by the use of modern highly parallelized platforms and software¹¹⁰ that could allow long ligand-mapping MD simulations of NMR-resolved protein structures to be completed within a few days.

The general applicability of this method was further demonstrated by using it to detect binding sites of hydrocarbon staples. These staples cross-link peptides intramolecularly and stabilize them against conformational heterogeneity for binding in a helical conformation to target proteins, as well as against proteolytic digestion. Hence, it is of great interest to develop methods that can help in their design. We tested the ligand-mapping protocol for its ability to detect hydrocarbon staple binding sites on five proteins with available structural data of bound stapled peptides that interact with the protein surface via their hydrocarbon staples. Employing benzenes as probes, the ligand-mapping MD simulations successfully detected the shallow hydrocarbon staple binding sites in all five proteins. In addition to reproducing the known staple interaction sites, the simulations also identified key hydrophobic interactions at the protein–peptide interface and yielded new sites for further exploration in these proteins. A novel second staple binding site that was predicted to form more extensive interactions with a hydrocarbon staple than a known site was identified in MCL-1. A stapled peptide binder of MCL-1 previously identified by library screening was modified to specifically target this region via its hydrocarbon staple. This design was supported by the results of free energy calculations derived from standard MD simulations of the complexes and also a previous computational study,¹⁰⁵ both of which suggest that the alternative stapled peptide MCL-1 SAHB_{8–12} binds to MCL-1 better than the original stapled peptide. This suggests that ligand-mapping MD simulations could complement staple-scanning MD simulations in the design of stapled peptides by highlighting hydrophobic regions close to the main peptide binding site where a hydrocarbon staple can interact with the protein.

Taken together, our current study demonstrates that ligand-mapping MD simulations hold immense potential as a tool with general applicability for detecting hydrophobic hot spots and hydrocarbon staple binding sites. The method could be used to suggest suitable mutations and modifications to improve the binding affinities of known peptide ligands, as well as inform the de novo design of peptidic PPI modulators. In cases of protein–protein and protein–peptide complexes with no resolved structures, the cutoff isovalue can be accordingly increased to initially locate high-affinity binding sites on the target protein. Peptide docking can then be restrained to these identified regions, obviating the need for a global docking search, which is time-consuming and generates many false positives.¹¹¹ However, further development is required to optimize the method for proper discrimination of low-affinity binding sites from irrelevant local energy minima, which is a common problem among MD-based mapping approaches.¹¹²

■ ASSOCIATED CONTENT

● Supporting Information

Structures of peptide-bound and unbound MCL-1 and MDM2; radial distribution function plots; tables of computed binding free energies. The Supporting Information is available free of charge on the ACS Publications website at DOI: 10.1021/ct5010577.

■ AUTHOR INFORMATION

Corresponding Author

*E-mail: chandra@bii.a-star.edu.sg.

Notes

The authors declare no competing financial interest.

■ ACKNOWLEDGMENTS

We are grateful for funding from BMSI, Agency for Science, Technology and Research (A*STAR). Y.S.T. was supported by an A*STAR Graduate Scholarship.

■ REFERENCES

- (1) Gerrard, J. A.; Hutton, C. A.; Perugini, M. A. Inhibiting protein-protein interactions as an emerging paradigm for drug discovery. *Mini-Rev. Med. Chem.* **2007**, *7*, 151–157.
- (2) Chene, P. Drugs targeting protein-protein interactions. *ChemMedChem* **2006**, *1*, 400–411.
- (3) Jones, S.; Thornton, J. M. Principles of protein-protein interactions. *Proc. Natl. Acad. Sci. U. S. A.* **1996**, *93*, 13–20.
- (4) Lo Conte, L.; Chothia, C.; Janin, J. The atomic structure of protein-protein recognition sites. *J. Mol. Biol.* **1999**, *285*, 2177–2198.
- (5) Craik, D. J.; Fairlie, D. P.; Liras, S.; Price, D. The future of peptide-based drugs. *Chem. Biol. Drug Des.* **2013**, *81*, 136–147.
- (6) Verdine, G. L.; Walensky, L. D. The challenge of drugging undruggable targets in cancer: lessons learned from targeting BCL-2 family members. *Clin. Cancer Res.* **2007**, *13*, 7264–7270.
- (7) Vlieghe, P.; Lisowski, V.; Martinez, J.; Khrestchatskiy, M. Synthetic therapeutic peptides: science and market. *Drug Discovery Today* **2010**, *15*, 40–56.
- (8) Maher, S.; Brayden, D. J.; Feighery, L.; McClean, S. Cracking the junction: update on the progress of gastrointestinal absorption enhancement in the delivery of poorly absorbed drugs. *Crit. Rev. Ther. Drug Carrier Syst.* **2008**, *25*, 117–168.
- (9) Patel, L. N.; Zaro, J. L.; Shen, W.-C. Cell penetrating peptides: intracellular pathways and pharmaceutical perspectives. *Pharm. Res.* **2007**, *24*, 1977–1992.
- (10) Maude, S.; Tai, L. R.; Davies, R. P. W.; Liu, B.; Harris, S. A.; Kocienski, P. J.; Aggeli, A. Peptide Synthesis and Self-Assembly. In *Peptide-Based Materials*; Deming, T., Ed.; Springer: Berlin, Germany, 2012; Vol. 310, pp 27–69.
- (11) Vagner, J.; Qu, H. C.; Hruby, V. J. Peptidomimetics, a synthetic tool of drug discovery. *Curr. Opin. Chem. Biol.* **2008**, *12*, 292–296.
- (12) Schafmeister, C. E.; Po, J.; Verdine, G. L. An all-hydrocarbon cross-linking system for enhancing the helicity and metabolic stability of peptides. *J. Am. Chem. Soc.* **2000**, *122*, 5891–5892.
- (13) Bruckdorfer, T.; Marder, O.; Albericio, F. From production of peptides in milligram amounts for research to multi-ton quantities for drugs of the future. *Curr. Pharm. Biotechnol.* **2004**, *5*, 29–43.
- (14) Blackwell, H. E.; Grubbs, R. H. Highly efficient synthesis of covalently cross-linked peptide helices by ring-closing metathesis. *Angew. Chem., Int. Ed.* **1998**, *37*, 3281–3284.
- (15) Verdine, G. L.; Hilinski, G. J. All-hydrocarbon stapled peptides as Synthetic Cell-Accessible Mini-Proteins. *Drug Discovery Today Technol.* **2012**, *9*, e41–e47.
- (16) Moellering, R. E.; Cornejo, M.; Davis, T. N.; Bianco, C. D.; Aster, J. C.; Blacklow, S. C.; Kung, A. L.; Gilliland, D. G.; Verdine, G. L.; Bradner, J. E. Direct inhibition of the NOTCH transcription factor complex. *Nature* **2009**, *462*, 182–188.

- (17) Bernal, F.; Tyler, A. F.; Korsmeyer, S. J.; Walensky, L. D.; Verdine, G. L. Reactivation of the p53 tumor suppressor pathway by a stapled p53 peptide. *J. Am. Chem. Soc.* **2007**, *129*, 2456–2457.
- (18) Walensky, L. D.; Kung, A. L.; Escher, I.; Malia, T. J.; Barbuto, S.; Wright, R. D.; Wagner, G.; Verdine, G. L.; Korsmeyer, S. J. Activation of apoptosis in vivo by a hydrocarbon-stapled BH3 helix. *Science* **2004**, *305*, 1466–1470.
- (19) Bhattacharya, S.; Zhang, H.; Debnath, A. K.; Cowburn, D. Solution structure of a hydrocarbon stapled peptide inhibitor in complex with monomeric C-terminal domain of HIV-1 capsid. *J. Biol. Chem.* **2008**, *283*, 16274–16278.
- (20) Zhang, H.; Zhao, Q.; Bhattacharya, S.; Waheed, A. A.; Tong, X.; Hong, A.; Heck, S.; Curreli, F.; Goger, M.; Cowburn, D.; Freed, E. O.; Ebner, A. K. A cell-penetrating helical peptide as a potential HIV-1 inhibitor. *J. Mol. Biol.* **2008**, *378*, 565–580.
- (21) Dhanal, N. N.; Walensky, L. D.; Zhang, C.-Y.; Choi, C. S.; Fisher, J. K.; Molina, A. J. A.; Datta, S. R.; Pitter, K. L.; Bird, G. H.; Wikstrom, J. D.; Deeney, J. T.; Robertson, K.; Morash, J.; Kulkarni, A.; Neschen, S.; Kim, S.; Greenberg, M. E.; Corkey, B. E.; Shirihai, O. S.; Shulman, G. I.; Lowell, B. B.; Korsmeyer, S. J. Dual role of proapoptotic BAD in insulin secretion and beta cell survival. *Nat. Med.* **2008**, *14*, 144–153.
- (22) Sviridov, D. O.; Ipkot, I. Z.; Stonik, J.; Drake, S. K.; Amar, M.; Osei-Hwedie, D. O.; Piszczek, G.; Turner, S.; Remaley, A. T. Helix stabilization of amphipathic peptides by hydrocarbon stapling increases cholesterol efflux by the ABCA1 transporter. *Biochem. Biophys. Res. Commun.* **2011**, *410*, 446–451.
- (23) Bird, G. H.; Boyapalle, S.; Wong, T.; Opoku-Nsiah, K.; Bedi, R.; Crannell, W. C.; Perry, A. F.; Nguyen, H.; Sampayo, V.; Devareddy, A.; Mohapatra, S.; Mohapatra, S. S.; Walensky, L. D. Mucosal delivery of a double-stapled RSV peptide prevents nasopulmonary infection. *J. Clin. Invest.* **2014**, *124*, 2113–2124.
- (24) Joseph, T. L.; Lane, D.; Verma, C. Stapled peptides in the p53 pathway: computer simulations reveal novel interactions of the staples with the target protein. *Cell Cycle* **2010**, *9*, 4560–4568.
- (25) Clackson, T.; Wells, J. A. A hot spot of binding energy in a hormone-receptor interface. *Science* **1995**, *267*, 383–386.
- (26) Bogan, A. A.; Thorn, K. S. Anatomy of hot spots in protein interfaces. *J. Mol. Biol.* **1998**, *280*, 1–9.
- (27) Bird, G. H.; Gavathiotis, E.; LaBelle, J. L.; Katz, S. G.; Walensky, L. D. Distinct BimBH3 (BimSAHB) stapled peptides for structural and cellular studies. *ACS Chem. Biol.* **2013**, *9*, 831–837.
- (28) Levitt, D. G.; Banaszak, L. J. POCKET: a computer graphics method for identifying and displaying protein cavities and their surrounding amino acids. *J. Mol. Graphics* **1992**, *10*, 229–234.
- (29) Goodford, P. J. A computational procedure for determining energetically favorable binding sites on biologically important macromolecules. *J. Med. Chem.* **1985**, *28*, 849–857.
- (30) Armon, A.; Graur, D.; Ben-Tal, N. ConSurf: an algorithmic tool for the identification of functional regions in proteins by surface mapping of phylogenetic information. *J. Mol. Biol.* **2001**, *307*, 447–463.
- (31) Konc, J.; Janežič, D. ProBiS algorithm for detection of structurally similar protein binding sites by local structural alignment. *Bioinformatics* **2010**, *26*, 1160–1168.
- (32) Tan, K. P.; Varadarajan, R.; Madhusudhan, M. S. DEPTH: a web server to compute depth and predict small-molecule binding cavities in proteins. *Nucleic Acids Res.* **2011**, *39*, W242–W248.
- (33) Teague, S. J. Implications of protein flexibility for drug discovery. *Nat. Rev. Drug Discovery* **2003**, *2*, 527–541.
- (34) Cozzini, P.; Kellogg, G. E.; Spyraakis, F.; Abraham, D. J.; Costantino, G.; Emerson, A.; Fanelli, F.; Gohlke, H.; Kuhn, L. A.; Morris, G. M.; Orozco, M.; Pertinhez, T. A.; Rizzi, M.; Sotriffer, C. A. Target flexibility: an emerging consideration in drug discovery and design. *J. Med. Chem.* **2008**, *51*, 6237–6255.
- (35) Eyrich, S.; Helms, V. Transient pockets on protein surfaces involved in protein-protein interaction. *J. Med. Chem.* **2007**, *50*, 3457–3464.
- (36) Schmidtke, P.; Bidon-Chanal, A.; Javier Luque, F.; Barril, X. MDpocket: open-source cavity detection and characterization on molecular dynamics trajectories. *Bioinformatics* **2011**, *27*, 3276–3285.
- (37) Guvench, O.; MacKerell, A. D., Jr. Computational fragment-based binding site identification by ligand competitive saturation. *PLoS Comp. Biol.* **2009**, *5*, e1000435.
- (38) Seco, J.; Luque, F. J.; Barril, X. Binding site detection and druggability index from first principles. *J. Med. Chem.* **2009**, *52*, 2363–2371.
- (39) Tan, Y. S.; Sledz, P.; Lang, S.; Stubbs, C. J.; Spring, D. R.; Abell, C.; Best, R. B. Using ligand-mapping simulations to design a ligand selectively targeting a cryptic surface pocket of polo-like kinase 1. *Angew. Chem., Int. Ed.* **2012**, *51*, 10078–10081.
- (40) Yang, C.-Y.; Wang, S. Hydrophobic binding hot spots of Bcl-xL protein-protein interfaces by cosolvent molecular dynamics simulation. *ACS Med. Chem. Lett.* **2011**, *2*, 280–284.
- (41) Bakan, A.; Nevins, N.; Lakdawala, A. S.; Bahar, I. Druggability assessment of allosteric proteins by dynamics simulations in the presence of probe molecules. *J. Chem. Theory Comput.* **2012**, *8*, 2435–2447.
- (42) Lexa, K. W.; Carlson, H. A. Full protein flexibility is essential for proper hot-spot mapping. *J. Am. Chem. Soc.* **2011**, *133*, 200–202.
- (43) Zhu, M.; De Simone, A.; Schenk, D.; Toth, G.; Dobson, C. M.; Vendruscolo, M. Identification of small-molecule binding pockets in the soluble monomeric form of the A β 42 peptide. *J. Chem. Phys.* **2013**, *139*, 035101.
- (44) Raman, E. P.; Yu, W.; Lakkaraju, S. K.; MacKerell, A. D., Jr. Inclusion of multiple fragment types in the site identification by ligand competitive saturation (SILCS) approach. *J. Chem. Inf. Model.* **2013**, *53*, 3384–3398.
- (45) Tan, Y. S.; Spring, D. R.; Abell, C.; Verma, C. The use of chlorobenzene as a probe molecule in molecular dynamics simulations. *J. Chem. Inf. Model.* **2014**, *54*, 1821–1827.
- (46) Stewart, M. L.; Fire, E.; Keating, A. E.; Walensky, L. D. The MCL-1 BH3 helix is an exclusive MCL-1 inhibitor and apoptosis sensitizer. *Nat. Chem. Biol.* **2010**, *6*, 595–601.
- (47) Phillips, C.; Roberts, L. R.; Schade, M.; Bazin, R.; Bent, A.; Davies, N. L.; Moore, R.; Pannifer, A. D.; Pickford, A. R.; Prior, S. H.; Read, C. M.; Scott, A.; Brown, D. G.; Xu, B.; Irving, S. L. Design and structure of stapled peptides binding to estrogen receptors. *J. Am. Chem. Soc.* **2011**, *133*, 9696–9699.
- (48) Baek, S.; Kutchukian, P. S.; Verdine, G. L.; Huber, R.; Holak, T. A.; Lee, K. W.; Popowicz, G. M. Structure of the stapled p53 peptide bound to Mdm2. *J. Am. Chem. Soc.* **2012**, *134*, 103–106.
- (49) Chang, Y. S.; Graves, B.; Guerlavais, V.; Tovar, C.; Packman, K.; To, K.-H.; Olson, K. A.; Kesavan, K.; Gangurde, P.; Mukherjee, A.; Baker, T.; Darlak, K.; Elkin, C.; Filipovic, Z.; Qureshi, F. Z.; Cai, H.; Berry, P.; Feyfant, E.; Shi, X. E.; Horstick, J.; Annis, D. A.; Manning, A. M.; Fotouhi, N.; Nash, H.; Vassilev, L. T.; Sawyer, T. K. Stapled α -helical peptide drug development: a potent dual inhibitor of MDM2 and MDMX for p53-dependent cancer therapy. *Proc. Natl. Acad. Sci. U. S. A.* **2013**, *110*, E3445–E3454.
- (50) Bayliss, R.; Sardon, T.; Vernos, I.; Conti, E. Structural basis of Aurora-A activation by TPX2 at the mitotic spindle. *Mol. Cell* **2003**, *12*, 851–862.
- (51) Pellegrini, L.; Yu, D. S.; Lo, T.; Anand, S.; Lee, M.; Blundell, T. L.; Venkiteraman, A. R. Insights into DNA recombination from the structure of a RAD51-BRCA2 complex. *Nature* **2002**, *420*, 287–293.
- (52) Uhrinova, S.; Uhrin, D.; Powers, H.; Watt, K.; Zheleva, D.; Fischer, P.; McInnes, C.; Barlow, P. N. Structure of free MDM2 N-terminal domain reveals conformational adjustments that accompany p53-binding. *J. Mol. Biol.* **2005**, *350*, 587–598.
- (53) Fire, E.; Gulla, S. V.; Grant, R. A.; Keating, A. E. Mcl-1-Bim complexes accommodate surprising point mutations via minor structural changes. *Protein Sci.* **2010**, *19*, 507–519.
- (54) Nettles, K. W.; Bruning, J. B.; Gil, G.; Nowak, J.; Sharma, S. K.; Hahm, J. B.; Kulp, K.; Hochberg, R. B.; Zhou, H.; Katzenellenbogen, J. A.; Katzenellenbogen, B. S.; Kim, Y.; Joachimiak, A.; Greene, G. L.

NFkB selectivity of estrogen receptor ligands revealed by comparative crystallographic analyses. *Nat. Chem. Biol.* **2008**, *4*, 241–247.

(55) Mocklinghoff, S.; Rose, R.; Carraz, M.; Visser, A.; Ottmann, C.; Brunsveld, L. Synthesis and crystal structure of a phosphorylated estrogen receptor ligand binding domain. *ChemBioChem* **2010**, *11*, 2251–2254.

(56) Kussie, P. H.; Gorina, S.; Marechal, V.; Elenbaas, B.; Moreau, J.; Levine, A. J.; Pavletich, N. P. Structure of the MDM2 oncoprotein bound to the p53 tumor suppressor transactivation domain. *Science* **1996**, *274*, 948–953.

(57) Czarna, A.; Popowicz, G. M.; Pecak, A.; Wolf, S.; Dubin, G.; Holak, T. A. High affinity interaction of the p53 peptide-analogue with human Mdm2 and Mdmx. *Cell Cycle* **2009**, *8*, 1176–1184.

(58) Fiser, A.; Sali, A. ModLoop: automated modeling of loops in protein structures. *Bioinformatics* **2003**, *19*, 2500–2501.

(59) Dolinsky, T. J.; Nielsen, J. E.; McCammon, J. A.; Baker, N. A. PDB2PQR: an automated pipeline for the setup of Poisson-Boltzmann electrostatics calculations. *Nucleic Acids Res.* **2004**, *32*, W665–W667.

(60) Martinez, L.; Andrade, R.; Birgin, E. G.; Martinez, J. M. PACKMOL: a package for building initial configurations for molecular dynamics simulations. *J. Comput. Chem.* **2009**, *30*, 2157–2164.

(61) Jorgensen, W. L.; Chandrasekhar, J.; Madura, J. D.; Impey, R. W.; Klein, M. L. Comparison of simple potential functions for simulating liquid water. *J. Chem. Phys.* **1983**, *79*, 926–935.

(62) Case, D. A.; Darden, T. A.; Cheatham, T. E.; Simmerling, C. L.; Wang, J.; Duke, R. E.; Luo, R.; Walker, R. C.; Zhang, W.; Merz, K. M.; Roberts, B.; Wang, B.; Hayik, S.; Roitberg, A.; Seabra, G.; Kolossvai, L.; Wong, K. F.; Paesani, F.; Vanicek, J.; Liu, J.; Wu, X.; Brozell, S. R.; Steinbrecher, T.; Gohlke, H.; Cai, Q.; Ye, X.; Wang, J.; Hsieh, M.-J.; Cui, G.; Roe, D. R.; Mathews, D. H.; Seetin, M. G.; Sagui, C.; Babin, V.; Luchko, T.; Gusarov, S.; Kovalenko, A.; Kollman, P. A. *AMBER 11*; University of California, San Francisco, CA, 2010.

(63) Lindorff-Larsen, K.; Piana, S.; Palmo, K.; Maragakis, P.; Klepeis, J. L.; Dror, R. O.; Shaw, D. E. Improved side-chain torsion potentials for the Amber ff99SB protein force field. *Proteins: Struct. Funct. Bioinform.* **2010**, *78*, 1950–1958.

(64) Wang, J. M.; Wolf, R. M.; Caldwell, J. W.; Kollman, P. A.; Case, D. A. Development and testing of a general amber force field. *J. Comput. Chem.* **2004**, *25*, 1157–1174.

(65) Vanqualef, E.; Simon, S.; Marquant, G.; Garcia, E.; Klimerak, G.; Delepine, J. C.; Cieplak, P.; Dupradeau, F.-Y. R.E.D. Server: a web service for deriving RESP and ESP charges and building force field libraries for new molecules and molecular fragments. *Nucleic Acids Res.* **2011**, *39*, W511–W517.

(66) Cornell, W. D.; Cieplak, P.; Bayly, C. I.; Kollman, P. A. Application of RESP charges to calculate conformational energies, hydrogen bond energies, and free energies of solvation. *J. Am. Chem. Soc.* **1993**, *115*, 9620–9631.

(67) Frisch, M. J.; Trucks, G. W.; Schlegel, H. B.; Scuseria, G. E.; Robb, M. A.; Cheeseman, J. R.; Scalmani, G.; Barone, V.; Mennucci, B.; Petersson, G. A.; Nakatsuji, H.; Caricato, M.; Li, X.; Hratchian, H. P.; Izmaylov, A. F.; Bloino, J.; Zheng, G.; Sonnenberg, J. L.; Hada, M.; Ehara, M.; Toyota, K.; Fukuda, R.; Hasegawa, J.; Ishida, M.; Nakajima, T.; Honda, Y.; Kitao, O.; Nakai, H.; Vreven, T.; Montgomery, J. A., Jr.; Peralta, J. E.; Ogliaro, F.; Bearpark, M.; Heyd, J. J.; Brothers, E.; Kudin, K. N.; Staroverov, V. N.; Kobayashi, R.; Normand, J.; Raghavachari, K.; Rendell, A.; Burant, J. C.; Iyengar, S. S.; Tomasi, J.; Cossi, M.; Rega, N.; Millam, N. J.; Klene, M.; Knox, J. E.; Cross, J. B.; Bakken, V.; Adamo, C.; Jaramillo, J.; Gomperts, R.; Stratmann, R. E.; Yazyev, O.; Austin, A. J.; Cammi, R.; Pomelli, C.; Ochterski, J. W.; Martin, R. L.; Morokuma, K.; Zakrzewski, V. G.; Voth, G. A.; Salvador, P.; Dannenberg, J. J.; Dapprich, S.; Daniels, A. D.; Farkas, Ö.; Foresman, J. B.; Ortiz, J. V.; Cioslowski, J.; Fox, D. J. *Gaussian 09, Revision B.1*; Gaussian, Inc.: Wallingford, CT, 2009.

(68) Meagher, K. L.; Redman, L. T.; Carlson, H. A. Development of polyphosphate parameters for use with the AMBER force field. *J. Comput. Chem.* **2003**, *24*, 1016–1025.

(69) Ryckaert, J. P.; Ciccotti, G.; Berendsen, H. J. C. Numerical integration of the Cartesian equations of motion of a system with

constraints: molecular dynamics of n-alkanes. *J. Comput. Phys.* **1977**, *23*, 327–341.

(70) Darden, T.; York, D.; Pedersen, L. Particle mesh Ewald: an $N \log(N)$ method for Ewald sums in large systems. *J. Chem. Phys.* **1993**, *98*, 10089–10092.

(71) Izaguirre, J. A.; Catarella, D. P.; Wozniak, J. M.; Skeel, R. D. Langevin stabilization of molecular dynamics. *J. Chem. Phys.* **2001**, *114*, 2090–2098.

(72) Berendsen, H. J. C.; Postma, J. P. M.; Vangunsteren, W. F.; Dinola, A.; Haak, J. R. Molecular dynamics with coupling to an external bath. *J. Chem. Phys.* **1984**, *81*, 3684–3690.

(73) DeLano, W. L. *The PyMOL Molecular Graphics System*; DeLano Scientific: San Carlos, CA, 2002.

(74) Liu, G.; Poppe, L.; Aoki, K.; Yamane, H.; Lewis, J.; Szyperki, T., High-quality NMR structure of human anti-apoptotic protein domain Mcl-1(171–327) for cancer drug design. *PLoS One* **2014**, *9*.

(75) Kollman, P. A.; Massova, I.; Reyes, C.; Kuhn, B.; Huo, S. H.; Chong, L.; Lee, M.; Lee, T.; Duan, Y.; Wang, W.; Donini, O.; Cieplak, P.; Srinivasan, J.; Case, D. A.; Cheatham, T. E. Calculating structures and free energies of complex molecules: combining molecular mechanics and continuum models. *Acc. Chem. Res.* **2000**, *33*, 889–897.

(76) Luo, R.; David, L.; Gilson, M. K. Accelerated Poisson-Boltzmann calculations for static and dynamic systems. *J. Comput. Chem.* **2002**, *23*, 1244–1253.

(77) Connolly, M. L. Analytical molecular surface calculation. *J. Appl. Crystallogr.* **1983**, *16*, 548–558.

(78) Brooks, B.; Karplus, M. Harmonic dynamics of proteins: normal modes and fluctuations in bovine pancreatic trypsin inhibitor. *Proc. Natl. Acad. Sci. U. S. A.* **1983**, *80*, 6571–6575.

(79) Gohlke, H.; Kiel, C.; Case, D. A. Insights into protein-protein binding by binding free energy calculation and free energy decomposition for the Ras-Raf and Ras-RaIGDS complexes. *J. Mol. Biol.* **2003**, *330*, 891–913.

(80) Rarey, M.; Kramer, B.; Lengauer, T.; Klebe, G. A fast flexible docking method using an incremental construction algorithm. *J. Mol. Biol.* **1996**, *261*, 470–489.

(81) Glaser, F.; Steinberg, D. M.; Vakser, I. A.; Ben-Tal, N. Residue frequencies and pairing preferences at protein-protein interfaces. *Proteins* **2001**, *43*, 89–102.

(82) Lexa, K. W.; Goh, G. B.; Carlson, H. A. Parameter choice matters: validating probe parameters for use in mixed-solvent simulations. *J. Chem. Inf. Model.* **2014**, *54*, 2190–2199.

(83) Mountzios, G.; Terpos, E.; Dimopoulos, M.-A. Aurora kinases as targets for cancer therapy. *Cancer Treat. Rev.* **2008**, *34*, 175–182.

(84) Cheng, Y.; Zhang, F.; Chen, Q.; Gao, J.; Cui, W.; Ji, M.; Tung, C.-H. Structural basis of specific binding between Aurora A and TPX2 by molecular dynamics simulations. *J. Chem. Inf. Model.* **2011**, *51*, 2626–2635.

(85) Gilis, D.; Biot, C.; Buisine, E.; Dehouck, Y.; Rooman, M. Development of novel statistical potentials describing cation- π interactions in proteins and comparison with semiempirical and quantum chemistry approaches. *J. Chem. Inf. Model.* **2006**, *46*, 884–893.

(86) Tateno, M.; Hagiwara, Y., Evaluation of stabilization energies in π - π and cation- π interactions involved in biological macromolecules by ab initio calculations. *J. Phys.: Condens. Matter* **2009**, *21*.

(87) Benson, F. E.; Stasiak, A.; West, S. C. Purification and characterization of the human Rad51 protein, an analogue of *E. coli* RecA. *EMBO J.* **1994**, *13*, 5764–5771.

(88) Baumann, P.; Benson, F. E.; West, S. C. Human Rad51 protein promotes ATP-dependent homologous pairing and strand transfer reactions in vitro. *Cell* **1996**, *87*, 757–766.

(89) Gupta, R. C.; Bazemore, L. R.; Golub, E. I.; Radding, C. M. Activities of human recombination protein Rad51. *Proc. Natl. Acad. Sci. U. S. A.* **1997**, *94*, 463–468.

(90) Yanagisawa, T.; Urade, M.; Yamamoto, Y.; Furuyama, J. Increased expression of human DNA repair genes, XRCC1, XRCC3 and RAD51, in radioresistant human KB carcinoma cell line N10. *Oral Oncol.* **1998**, *34*, 524–528.

(91) Maacke, H.; Jost, K.; Opitz, S.; Miska, S.; Yuan, Y.; Hasselbach, L.; Luttes, J.; Kalthoff, H.; Sturzbecher, H. W. DNA repair and recombination factor Rad51 is over-expressed in human pancreatic adenocarcinoma. *Oncogene* **2000**, *19*, 2791–2795.

(92) Maacke, H.; Opitz, S.; Jost, K.; Hamdorf, W.; Henning, W.; Kruger, S.; Feller, A. C.; Lopens, A.; Diedrich, K.; Schwinger, E.; Sturzbecher, H. W. Over-expression of wild-type Rad51 correlates with histological grading of invasive ductal breast cancer. *Int. J. Cancer* **2000**, *88*, 907–913.

(93) Chen, P. L.; Chen, C. F.; Chen, Y. M.; Xiao, J.; Sharp, Z. D.; Lee, W. H. The BRC repeats in BRCA2 are critical for RAD51 binding and resistance to methyl methanesulfonate treatment. *Proc. Natl. Acad. Sci. U. S. A.* **1998**, *95*, 5287–5292.

(94) Wong, A. K. C.; Pero, R.; Ormonde, P. A.; Tavtigian, S. V.; Bartel, P. L. RAD51 interacts with the evolutionarily conserved BRC motifs in the human breast cancer susceptibility gene *brca2*. *J. Biol. Chem.* **1997**, *272*, 31941–31944.

(95) Rajendra, E.; Venkitaraman, A. R. Two modules in the BRC repeats of BRCA2 mediate structural and functional interactions with the RAD51 recombinase. *Nucleic Acids Res.* **2010**, *38*, 82–96.

(96) Cole, D. J.; Rajendra, E.; Roberts-Thomson, M.; Hardwick, B.; McKenzie, G. J.; Payne, M. C.; Venkitaraman, A. R.; Skylaris, C.-K., Interrogation of the protein-protein interactions between human BRCA2 BRC repeats and RAD51 reveals atomistic determinants of affinity. *PLoS Comp. Biol.* **2011**, *7*.

(97) Scott, D. E.; Ehebauer, M. T.; Pukala, T.; Marsh, M.; Blundell, T. L.; Venkitaraman, A. R.; Abell, C.; Hyvoenen, M. Using a fragment-based approach to target protein-protein interactions. *ChemBioChem* **2013**, *14*, 332–342.

(98) Henzler-Wildman, K.; Kern, D. Dynamic personalities of proteins. *Nature* **2007**, *450*, 964–972.

(99) Brown, C. J.; Lain, S.; Verma, C. S.; Fersht, A. R.; Lane, D. P. Awakening guardian angels: drugging the p53 pathway. *Nat. Rev. Cancer* **2009**, *9*, 862–873.

(100) Bottger, A.; Bottger, V.; Garcia-Echeverria, C.; Chene, P.; Hochkeppel, H. K.; Sampson, W.; Ang, K.; Howard, S. F.; Picksley, S. M.; Lane, D. P. Molecular characterization of the hdm2-p53 interaction. *J. Mol. Biol.* **1997**, *269*, 744–756.

(101) Showalter, S. A.; Bruschweiler-Li, L.; Johnson, E.; Zhang, F.; Bruschweiler, R. Quantitative lid dynamics of MDM2 reveals differential ligand binding modes of the p53-binding cleft. *J. Am. Chem. Soc.* **2008**, *130*, 6472–6478.

(102) Vassilev, L. T.; Vu, B. T.; Graves, B.; Carvajal, D.; Podlaski, F.; Filipovic, Z.; Kong, N.; Kammlott, U.; Lukacs, C.; Klein, C.; Fotouhi, N.; Liu, E. A. In vivo activation of the p53 pathway by small-molecule antagonists of MDM2. *Science* **2004**, *303*, 844–848.

(103) Hernychova, L.; Man, P.; Verma, C.; Nicholson, J.; Sharma, C.-A.; Ruckova, E.; Teo, J. Y.; Ball, K.; Vojtesek, B.; Hupp, T. R. Identification of a second Nutlin-3 responsive interaction site in the N-terminal domain of MDM2 using hydrogen/deuterium exchange mass spectrometry. *Proteomics* **2013**, *13*, 2512–2525.

(104) Lessene, G.; Czabotar, P. E.; Colman, P. M. BCL-2 family antagonists for cancer therapy. *Nat. Rev. Drug Discovery* **2008**, *7*, 989–1000.

(105) Joseph, T. L.; Lane, D. P.; Verma, C. S. Stapled BH3 peptides against MCL-1: mechanism and design using atomistic simulations. *PLoS One* **2012**, *7*, e43985.

(106) Tora, L.; White, J.; Brou, C.; Tasset, D.; Webster, N.; Scheer, E.; Chambon, P. The human estrogen receptor has two independent nonacidic transcriptional activation functions. *Cell* **1989**, *59*, 477–487.

(107) Brzozowski, A. M.; Pike, A. C. W.; Dauter, Z.; Hubbard, R. E.; Bonn, T.; Engstrom, O.; Ohman, L.; Greene, G. L.; Gustafsson, J.-A.; Carlquist, M. Molecular basis of agonism and antagonism in the oestrogen receptor. *Nature* **1997**, *389*, 753–758.

(108) Heery, D. M.; Kalkhoven, E.; Hoare, S.; Parker, M. G. A signature motif in transcriptional co-activators mediates binding to nuclear receptors. *Nature* **1997**, *387*, 733–736.

(109) Shiau, A. K.; Barstad, D.; Loria, P. M.; Cheng, L.; Kushner, P. J.; Agard, D. A.; Greene, G. L. The structural basis of estrogen

receptor/coactivator recognition and the antagonism of this interaction by tamoxifen. *Cell* **1998**, *95*, 927–937.

(110) Salomon-Ferrer, R.; Goetz, A. W.; Poole, D.; Le Grand, S.; Walker, R. C. Routine microsecond molecular dynamics simulations with AMBER on GPUs. 2. Explicit solvent particle mesh Ewald. *J. Chem. Theory Comput.* **2013**, *9*, 3878–3888.

(111) Ritchie, D. W. Recent progress and future directions in protein-protein docking. *Curr. Protein Peptide Sci.* **2008**, *9*, 1–15.

(112) Lexa, K. W.; Carlson, H. A. Improving protocols for protein mapping through proper comparison to crystallography data. *J. Chem. Inf. Model.* **2013**, *53*, 391–402.